

Nanoscale Surface Mechanical Property Measurements: Force Modulation Techniques Applied to Nanoindentation

S.A. Syed Asif¹, R.J. Colton², and K.J. Wahl²

¹Department of Materials Science, University of Florida, Gainesville, FL 32611

²Code 6170, Naval Research Laboratory, Washington DC 20375

Mechanical properties of surfaces and interfaces are important for understanding the behavior of adhesive and sliding contacts, where changes in interfacial properties can result from surface treatments, sliding processes, or contaminants. Recent advances combining nanoindentation, atomic force microscopy and force modulation techniques enable examination of surface mechanical properties with substantially improved force and spatial resolution, and enable *quantitative, dynamic* measurements of surface mechanical properties of nanoscale contacts. We present examples demonstrating quantitative, surface sensitive nanomechanics of thin films and compliant polymers, damping losses and the effects of water vapor. Additionally, we present a new, quantitative stiffness imaging technique for mechanical properties mapping at the nanoscale.

Materials properties measurements at submicron scales are important not only for characterization of ever smaller electronic and mechanical devices, but also for analyses of thin interfacial films controlling friction and adhesion. Two types of instruments have been developed to facilitate studies of thin films with high spatial resolution: the depth-sensing nanoindenter (1) and the atomic force microscope (AFM) (2). Capabilities of both instruments have been extended through the use of AC modulation techniques, enabling continuous measurement of contact stiffness (3-6), enhanced imaging capabilities (7), and examination of polymer creep and viscoelastic properties (8,9), for example. While both instruments can be used to determine materials properties at the nanoscale, there are distinct advantages and disadvantages to both techniques. New approaches coupling AFM and depth-sensing nanoindentation (10-12), which we will refer to as hybrid nanoindentation, can provide the best of both techniques. In this paper, we will discuss these approaches, as well as present recent progress and examples from work carried out at NRL to

| Report Documentation Page | | | Form Approved OMB No. 0704-0188 | | |
|--|------------------------------------|-------------------------------------|--|---|---------------------------------|
| Public reporting burden for the collection of information is estimated to average 1 hour per response, including the time for reviewing instructions, searching existing data sources, gathering and maintaining the data needed, and completing and reviewing the collection of information. Send comments regarding this burden estimate or any other aspect of this collection of information, including suggestions for reducing this burden, to Washington Headquarters Services, Directorate for Information Operations and Reports, 1215 Jefferson Davis Highway, Suite 1204, Arlington VA 22202-4302. Respondents should be aware that notwithstanding any other provision of law, no person shall be subject to a penalty for failing to comply with a collection of information if it does not display a currently valid OMB control number. | | | | | |
| 1. REPORT DATE 2000 | | 2. REPORT TYPE | | 3. DATES COVERED 00-00-2000 to 00-00-2000 | |
| 4. TITLE AND SUBTITLE Nanoscale Surface Mechanical Property Measurements: Force Modulation Techniques Applied to Nanoindentation | | | 5a. CONTRACT NUMBER | | |
| | | | 5b. GRANT NUMBER | | |
| | | | 5c. PROGRAM ELEMENT NUMBER | | |
| 6. AUTHOR(S) | | | 5d. PROJECT NUMBER | | |
| | | | 5e. TASK NUMBER | | |
| | | | 5f. WORK UNIT NUMBER | | |
| 7. PERFORMING ORGANIZATION NAME(S) AND ADDRESS(ES) Naval Research Laboratory, Code 6170, 4555 Overlook Avenue, SW, Washington, DC, 20375 | | | 8. PERFORMING ORGANIZATION REPORT NUMBER | | |
| 9. SPONSORING/MONITORING AGENCY NAME(S) AND ADDRESS(ES) | | | 10. SPONSOR/MONITOR'S ACRONYM(S) | | |
| | | | 11. SPONSOR/MONITOR'S REPORT NUMBER(S) | | |
| 12. DISTRIBUTION/AVAILABILITY STATEMENT Approved for public release; distribution unlimited | | | | | |
| 13. SUPPLEMENTARY NOTES The original document contains color images. | | | | | |
| 14. ABSTRACT | | | | | |
| 15. SUBJECT TERMS | | | | | |
| 16. SECURITY CLASSIFICATION OF: | | | 17. LIMITATION OF ABSTRACT | 18. NUMBER OF PAGES 18 | 19a. NAME OF RESPONSIBLE PERSON |
| a. REPORT unclassified | b. ABSTRACT unclassified | c. THIS PAGE unclassified | | | |

develop surface sensitive, quantitative nanoscale mechanical property analyses for thin films and polymer surfaces.

Background: Mechanical Properties Measurements via Nanoindentation

Indentation has been used for over 100 years to determine hardness of materials (13). For a given indenter geometry (e.g. spherical or pyramidal), hardness is determined by the ratio of the applied load to the projected area of contact, determined optically after indentation. Interest in properties of materials with smaller dimensionality (e.g. thin films and microstructures) required lower load indentation and a new way of determining the indent size, due to optical limitations. Depth-sensing nanoindentation (1) was developed to eliminate the need to visualize the indents, and resulted in the added capability of measuring properties like elastic modulus, E , and creep.

DC Techniques

Depth-Sensing Nanoindentation

For depth-sensing nanoindentation, a controlled, variable force is applied to a sample by the indenter and the resulting displacement of the indenter is measured. The resulting “load vs. displacement” data, together with the indenter geometry, can be analyzed to obtain hardness and elastic modulus using well established mechanical models (14). The simultaneous measurement of load and displacement also allows study of creep (time dependent strain response due to a step change in stress) (15,16).

In general, the instrument configuration for depth-sensing nanoindentation is a parallel plate geometry sandwiching a plate held by leaf springs between two rigid, parallel plates (Fig. 1a). A diamond indenter tip, attached to a shaft, is mounted to the middle plate, and is accommodated by a small hole in the center of the lowest plate. A force, F , is generated by applying a voltage between the middle plate by the bottom

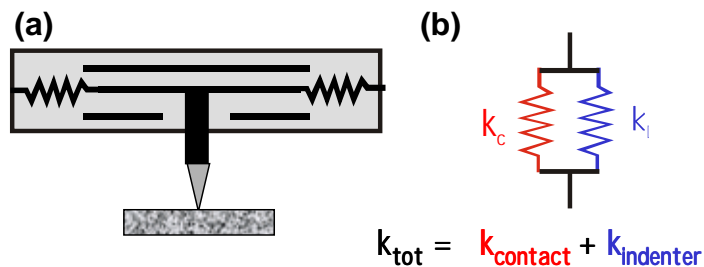


Figure 1. (a) indenter model and (b) simple mechanical model for force controlled indentation assuming purely elastic mechanics.

plate through electrostatic actuation, and the resulting displacement measured by change in capacitance between the middle plate and the outer plates. An advantage of force-controlled operation is that indentation is not limited to contacts with lower stiffness than the indenter spring stiffness, since the force is applied to the indenter against the spring by electrostatics; the simple mechanical model (two springs in parallel) is shown in Fig. 1b.

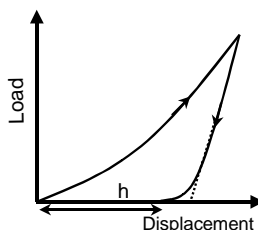


Figure 2. Typical load-displacement graph for elasto-plastic indentation.

A typical load-displacement curve is shown in Fig. 2. The loading portion of the curve results from both plastic and elastic deformation response of the contact, while the unloading portion of the curve is related to the elastic recovery of the contact. If the indenter geometry and materials properties are known, the modulus can be obtained by fitting the unloading curve to determine the contact stiffness at maximum load (14, 17). In this case,

$$E^* = \frac{\sqrt{\pi} \cdot \text{slope}}{2\sqrt{A}} \quad (1)$$

where E^* is the reduced modulus ($E^* = [(1-\nu_1^2)/E_1 + (1-\nu_2^2)/E_2]^{-1}$) and A is the projected contact area determined from indenter geometry and penetration depth. Generally, the hardness can be determined by measuring the residual contact depth, h , to determine A (14).

AFM-Based Nanoindentation

Mechanical properties of materials can also be obtained through analyses of force-distance curves generated with an AFM. In the AFM, measurements are displacement controlled – the sample is displaced against a cantilever indenter via a piezoelectric actuator – and forces are inferred from the measured deflection of the cantilever and its (nominally) known spring constant. Several different cantilever configurations and displacement detection schemes have been used for these measurements (Fig. 3a) (18). Early work by Burnham and Colton (19) employed double beam and crossed beam spring configurations, with spring deflection measured via STM tunneling current. More recently, simple diving-board cantilevers and optical detection are being used (20-22). Because the AFM uses displacement control configuration, the simple mechanical model is that of two springs in series (Fig. 3b). This simple difference has several ramifications for indentation via AFM. First, the indenter spring stiffness must be matched to the contact stiffness in order to get a

measurable deformation in the sample itself, rather than simple deflection of the cantilever spring. Secondly, depth of penetration (and projected contact area), for all but the most compliant materials, is difficult to determine due to piezo creep and hysteresis effects (23).

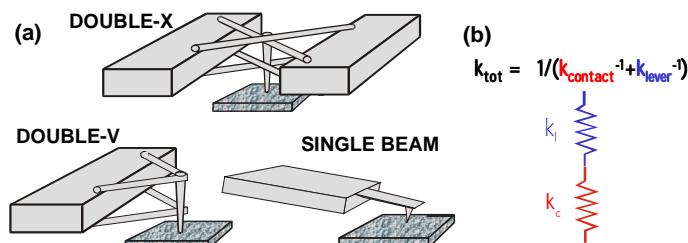


Figure 3 (a) Various AFM cantilever configurations for indentation experiments and (b) simple mechanical model for AFM indentation (by sample displacement).

Trends in the unloading slopes of force-distance curves for various materials pairs examined (gold/nickel, diamond/graphite, diamond/diamond) were consistent with expected relative reduced moduli (Fig. 4) (24). However, because of the difficulty in determining indenter penetration relative to the sample surface for these relatively stiff materials, only qualitative results could be obtained. Semi-quantitative measurements may be possible under certain circumstances (e.g. compliant elastomers) (22) where tip penetration into the sample is significant. However, the indentation geometries involving non-perpendicular tip-sample approach result in significant lateral force

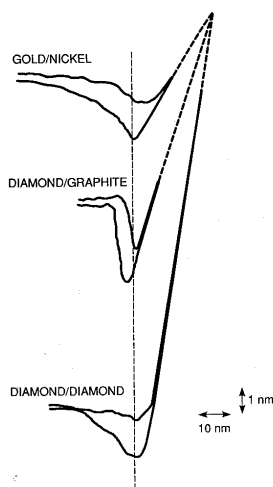


Figure 4. AFM force curves showing slope differences for different material pairs Reprinted with permission from reference (24). Copyright 1994 Institute of Physics.

contributions during indentation (evidenced by asymmetrical indents) (20). Additionally, the compliant materials systems accessible with this approach often have significant time-dependent materials properties (e.g. creep relaxation and viscoelastic behavior) that complicate (and even prevent) analyses of mechanical properties from simple force-displacement curves (25).

AC Modulation Techniques

Depth-Sensing Nanoindentation

By adding a small AC modulation to the force during experiments, and monitoring displacement with a lock-in amplifier, Pethica and Oliver (3) demonstrated they could obtain contact stiffness ($\partial F/\partial x$) continuously throughout the indentation. Hardness and modulus vs. depth information, as well as tip characterization, previously obtained by performing multiple indents and analyzing unloading slopes at many different depths, could be performed in one single experiment. Quantification of the data depends on obtaining accurate dynamic characterization of the instrument (dynamic response vs. frequency), and applying an appropriate dynamic mechanical model (3).

The addition of AC force modulation to the nanoindentation measurements increases sensitivity to elasto-plastic deformation and creep, as well as enables examination of damping or loss properties of materials, critical for determining mechanical properties of polymers (8).

AFM-Based Nanoindentation

AC modulation techniques have become commonplace in AFM instrumentation over the last few years, in many cases for the enhanced imaging capabilities it affords. All but one of these modulation techniques involve displacement modulation, either of the sample (z-modulation) (26-29) or of the tip holder - depending on frequency of modulation, so-called “tapping mode” near cantilever resonance but above feedback frequency (30). The appropriate dynamic mechanical models and responses for these systems are reviewed by Burnham et al. (31). Quantitative analysis of mechanical properties from these techniques has been attempted (29,32,33), but is complicated due to displacement (not force) modulation and difficulty of knowing contact area. Jarvis et al. (34,35) demonstrated force modulation with AFM using a current carrying coil and permanent magnet affixed to the end of a cantilever; therefore the models described above for depth-sensing nanoindentation are applicable, although cantilever calibration and approach angle may be problematic. This is the only technique using AFM cantilevers that truly involves *force* modulation; all the other methods involve displacement modulation (31), but are often misrepresented as force modulation in the literature.

Experimental Procedures and Equipment

Our recent work at the Naval Research Laboratory (NRL) has focused on developing quantitative mechanical properties measurements using hybrid nanoindentation techniques that couple depth sensing nanoindentation with AFM sample positioning and imaging capabilities. Hybrid indentation provides significant advantages over traditional (force controlled) and AFM-based (displacement controlled) nanoindentation instrumentation, eliminating many of the weaknesses of either technique. Specifically, depth-sensing nanoindentation provides accurate load control, high displacement accuracy, and normal (perpendicular) sample loading, while the AFM scanner electronics provide high lateral resolution and imaging. The experiments described in this work have been performed with a Hysitron, Inc. Triboscope nanoindenter coupled with a Digital Instruments Nanoscope IIIa AFM. We have modified the instrumentation to enable AC force modulation by adding a lock-in amplifier, voltage summing electronics, amplifier and break-out boxes (Fig. 5) (12).

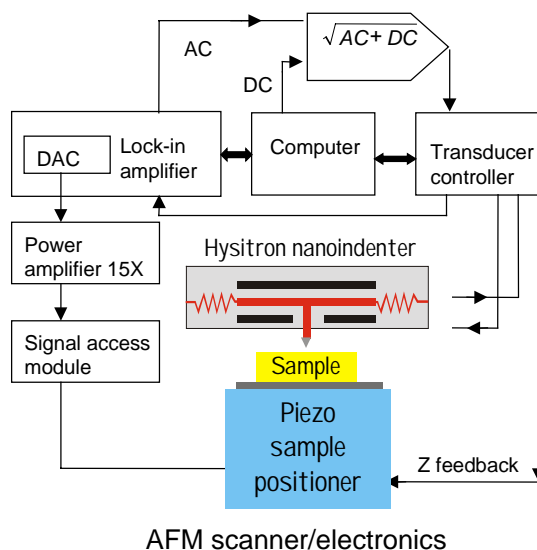


Figure 5. Schematic diagram of hybrid nanoindenter apparatus.

Detailed explanations of AC force modulation techniques and analyses can be found in the literature (3,8,12). Briefly, for a superimposed force $F = F_o \sin \omega t$, there is a corresponding steady-state displacement oscillation at the same frequency given by $x = X_o \sin (\omega t - \phi)$. Using the dynamic model shown in Fig. 6a, an analytical solution for the resulting displacement amplitude, X_o , and phase shift, ϕ , can be found

if the machine frame stiffness is assumed to be infinite. The solution for displacement amplitude is

$$X_o = \frac{F_o}{\sqrt{(k - m\omega^2)^2 + [(C_i + C_s)\omega]^2}} \quad (2)$$

and phase shift between the applied force and measured displacement is

$$\phi = \tan^{-1} \frac{(C_i + C_s)\omega}{k - m\omega^2} \quad (3)$$

where ω is the frequency in rad/s, C_i is the damping coefficient of the air gap in the displacement transducer, m is the indenter mass, and C_s is the damping coefficient of the sample. The combined stiffness of the sample and indenter, k , is given by

$$k = K_s + K_i \quad (4)$$

where K_s is the sample stiffness and K_i is the indenter spring stiffness. The contact stiffness, $k = (\partial F / \partial x) = F_o / X_o$, at any point in an indentation experiment is given by equation (1), where *slope* is replaced by stiffness k . Thus if either the sample's modulus, E , or contact area, A , is known, the other can be determined from this relationship (14); if the modulus is known the hardness can also be measured. Viscoelastic materials that can damp the AC force have both storage K'_s (in phase) and loss $K''_s = \omega C_s$ (90° out of phase) components of stiffness; if both are known then storage and loss moduli can be obtained from eq. (1).

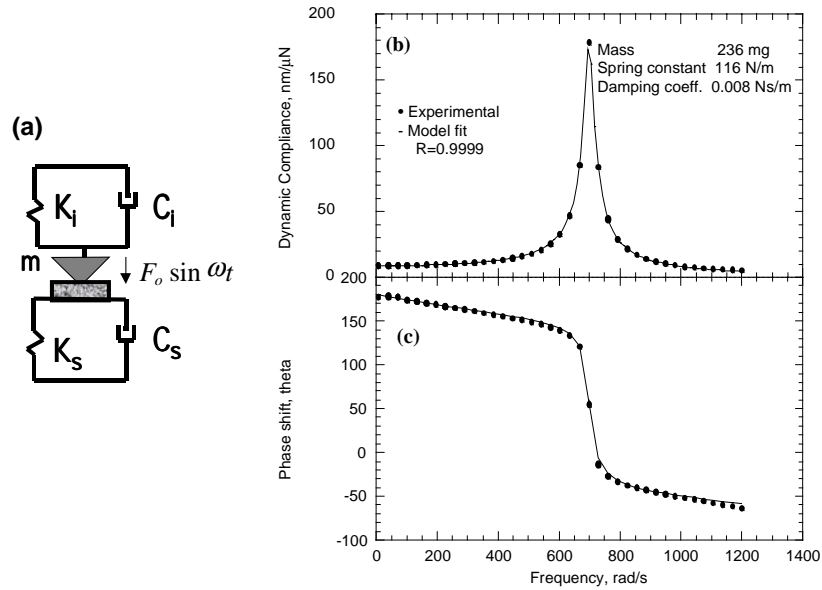


Figure 6. (a) Dynamic model (see accompanying text), (b) dynamic compliance and (c) phase response of the freely suspended indenter. Reprinted with permission from reference (12). Copyright 1999 American Institute of Physics.

Figure 6b and c shows the dynamic compliance and corresponding phase shift of the indenter (uncorrected for electronics). The response was fit to the model in Fig. 6a; for this indenter the damping coefficient, C_i is 0.008 Ns/m, resonance frequency, ω_0 is 110 Hz, indenter mass, m is 236 mg, and spring constant, K_i is 116 N/m. A Berkovich diamond indenter with a tip radius of ~ 200 nm was used for all experiments. Tip shape calibration and machine compliance were determined by standard techniques (14) using electropolished indium and quartz.

Results and Discussion

DC vs. AC Measurements

There are often several methods for measuring the same mechanical properties. As mentioned previously, AC techniques provide the added advantages of enabling time-dependent measurements like damping loss and creep as well as enhancing sensitivity. Here we provide two examples of how AC force modulation contributes information not available through more standard DC experiments.

Spring Stiffness and Damping Loss

Spring stiffness measurements are a good example to illustrate and compare the DC and AC measurement techniques described above. Figure 7 shows a force-displacement curve for the indenter against the end of a small Ta cantilever attached

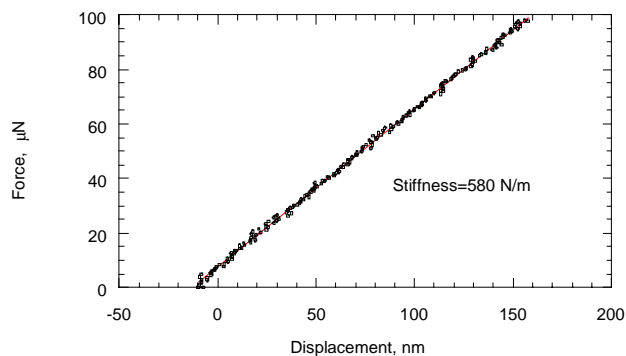


Figure 7. Load-displacement data for tantalum cantilever. The slope is the combined stiffness of the cantilever and indenter; lever stiffness was measured as 580 N/m. Reprinted with permission from reference (12). Copyright 1999 American Institute of Physics.

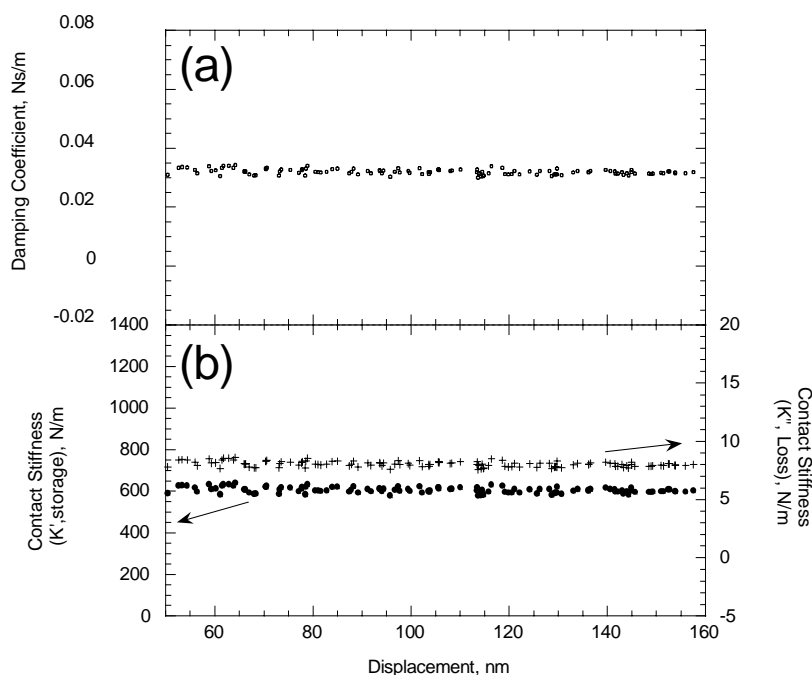


Figure 8. (a) Damping coefficient and (b) stiffness (storage and loss components) of tantalum cantilever glued to glass substrate. Reprinted with permission from reference (12). Copyright 1999 American Institute of Physics.

to a glass substrate via superglue (12). The stiffness of the Ta cantilever was determined by subtracting the indenter spring stiffness (116 N/m) from the slope of the force-displacement curve, and found to be 580 N/m ($r=0.98$).

For comparison, AC measurements were made using an AC force of 300 nN at 40 Hz during loading and unloading. Interestingly, the measured phase shift and amplitude of the AC displacement response revealed that the cantilever, which was expected to behave like an ideal spring, was actually damped. Figure 8a shows the damping coefficient as a function of displacement using Eq. (3); the main source of damping was likely the glue used to mount the lever on the substrate. Storage and loss components of stiffness were also calculated from the data, and are shown in Fig. 8b. The storage component of the stiffness was 600 ± 10 N/m, in agreement with that measured by the DC technique. The loss component was about 8 ± 1 N/m, demonstrating the importance of rigidly mounting samples for nanoindentation experiments so as not to influence the mechanical response of the system under investigation. The sensitivity of the AC technique is about 0.1 N/m, enabling spring constant determination of small levers used by the AFM and micro-electromechanical systems (MEMS) communities.

Low Modulus Polymer Mechanical Properties

Measuring the mechanical properties of very compliant materials by indentation is difficult because the indenter springs are generally several orders of magnitude stiffer than the contact stiffness. Larger contact areas (e.g. spherical indenters) can be used, but that may defeat the purpose by reducing lateral resolution significantly. The upper plot in Fig. 9 shows the DC load-displacement curve for an indentation against poly-isoprene. The data are linear, demonstrating elastic behavior of the contact, with a slope of 117 ± 1 N/m. However, the stiffness of the indenter itself is 116 N/m, and subtracting this value to obtain the contact stiffness (Eq. 4) leaves a value within the uncertainty of the measurement. By making the same measurement, but adding AC force modulation (AC force of 300 nN at 40 Hz), the contact stiffness throughout the load-displacement curve was obtained (Fig. 9, lower plot). Using experimentally determined tip shape data and a literature value for Poisson's ratio (36), the elastic modulus of the poly-isoprene sample was found to be 1.1 ± 0.4 MPa. This compares favorably with other values found in the literature (36,37).

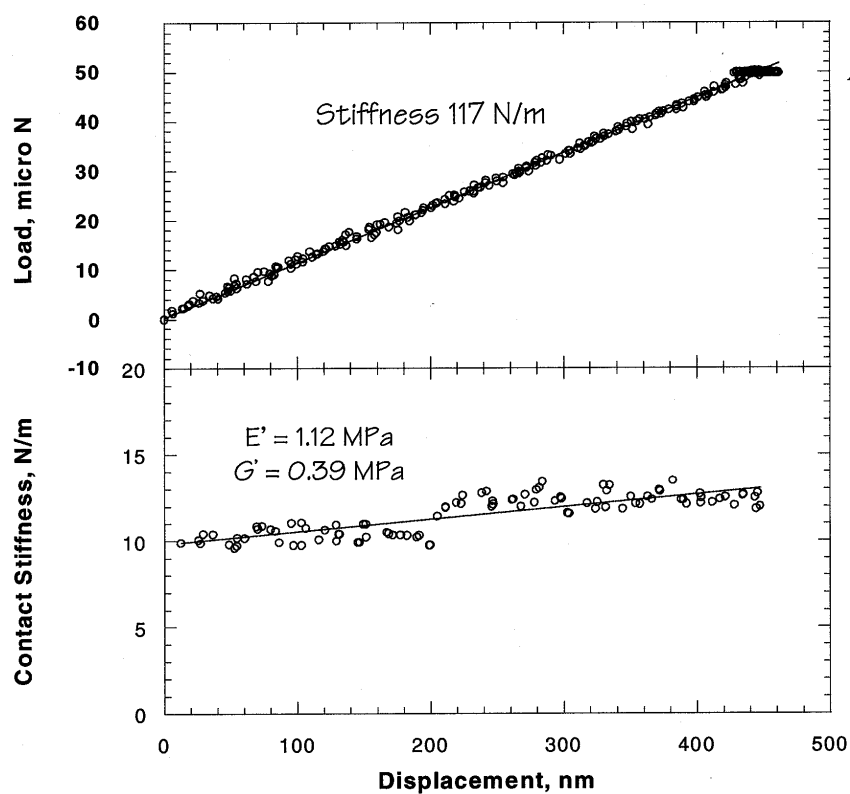


Figure 9. Load-displacement data and contact stiffness for poly-isoprene.

Surface Spectroscopy – Force/Stiffness Measurements and Imaging

Surface Sensitivity and Finding the Surface

One of the challenges in nanoindentation involves detecting the sample surface (before indentation): specimens may undergo damage on approach, and very compliant samples might not be sensed at all (as in the case shown in Fig. 9). Monitoring the dynamic response of the nanoindenter during tip-sample approach provides a very sensitive way to determine the location of the surface prior to indentation and provides a mode of force-distance curve acquisition (12,38). Due to the large phase shift at resonance (Fig. 6), any change in dynamic compliance due to tip-surface interaction results in a large phase shift. For example, if the indenter driving (AC force modulation) frequency is slightly less than the resonance frequency (110 Hz) during the tip-specimen approach, an increasing attractive force (positive force gradient) shifts the resonance frequency to lower frequency. The attractive force results in increased dynamic compliance (decreased stiffness) and decrease in phase (Fig. 6). If the tip-sample distance is decreased further, repulsive interactions can also be sensed by increased interaction stiffness and increased phase shift.

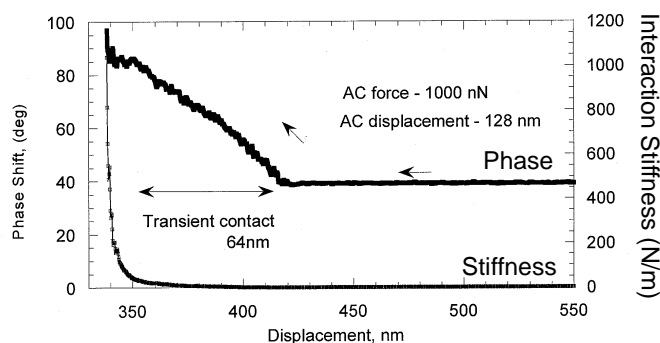


Figure 10. Tip-sample approach curve showing phase response and calculated interaction stiffness.

An example of this approach to finding a sample surface is shown in Fig. 10 above. In this case, a large AC force of 1000 nN was applied to the indenter spring, and the tip-surface separation controlled by the AFM piezo. When the tip and sample begin to interact, significant shifts in the phase are observed, and eventually a sharp increase in phase is observed. Interaction stiffness was calculated from the amplitude and phase response and is shown in the same plot. From this it can be seen that the sharp increase in phase occurs after the sharp increase in contact stiffness. There is a large region of "transient contact" (~64 nm) due to the large AC force used which resulted in a 64 nm displacement amplitude (128 nm total displacement) of the tip. Using much smaller AC forces results in more sensitive surface detection and reduced transient contact. By monitoring the phase shift during the force-distance approach,

one can choose to retract the tip at any point, producing a force-curve and interaction stiffness curve. This allows adhesive and repulsive interactions to be examined more directly.

We have used the above approach to examine pre-contact and apparent contact regimes for various ceramic, metallic and polymer surfaces. An example of stiffness interaction and force curves for a Si surface with a native oxide at ~56% relative humidity (RH) is shown in Fig. 11. The AC force is ~20 nN. The stiffness data initially show a downward deflection (negative with respect to the cantilever stiffness, which has been subtracted) indicating an adhesive interaction between the tip and substrate. The stiffness soon turns positive, and upon retraction shows significant hysteresis; the hysteresis is due to a real change in contact area from surface deformation and is not an experimental artifact. The corresponding force-displacement curve shows that the maximum force during indentation was 300 nN, and confirms that even at this low load that the unloading was not reversible and the deformation not elastic. The negative stiffness and adhesive force observed during retraction is consistent with capillary condensation (39). Estimation of surface energy from this data set and others gave results between 60 and 80 mJ/m (38), consistent with the surface energy of water (72 mJ/m) (39).

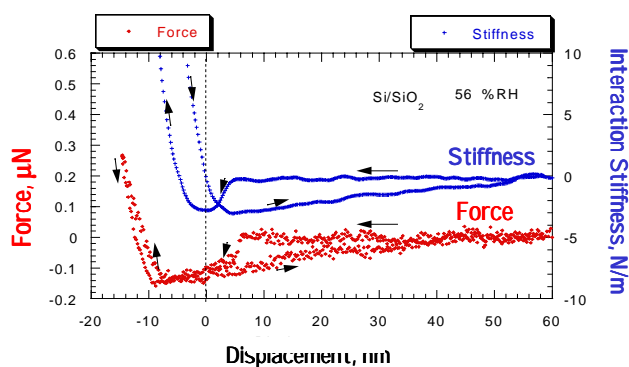


Figure 11. Force and interaction stiffness curves during approach (\leftarrow) and retraction (\rightarrow) (38).

The data in Fig. 11 show an offset between the force and stiffness minima in the approach and retraction curves. The explanation for this is shown in Fig. 12, which illustrates the relationship between potential, force and interaction stiffness. These curves provide a basis for determining where the contact point with the surface is located. One definition of contact is the position on the curve where the repulsive force can first be detected (*see* 24), typically identified by a change in curvature of the force-displacement data (3). Therefore, the force gradient (stiffness-displacement data) reveals more clearly the attractive to repulsive transition. The initiation of repulsive contact is thus found from the minimum of the stiffness approach curve (marked at 0 nm), which marks the maximum attractive interaction stiffness. The stiffness data represent a convolution of force gradient and contact stiffness and is

therefore not as narrow as expected for a true evaluation of surface potential; sharper tips and better force resolution are needed for such a measurement.

Finally, for most surfaces we have examined, the maximum interaction stiffness is not greater than the nanoindenter spring stiffness. This allows the attractive part of the

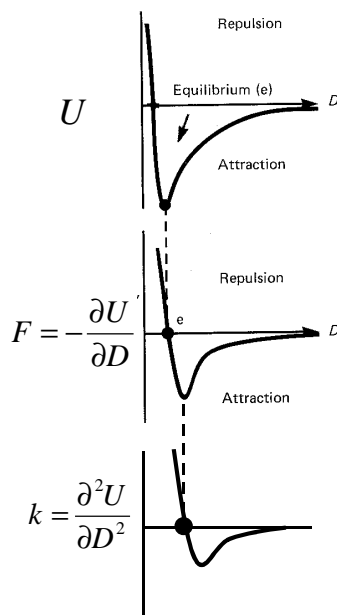


Figure 12. (a) Surface potential, (b) potential gradient (force), and (c) force gradient (stiffness). Adapted with permission from reference (40). Copyright 1991 Academic Press, Inc.

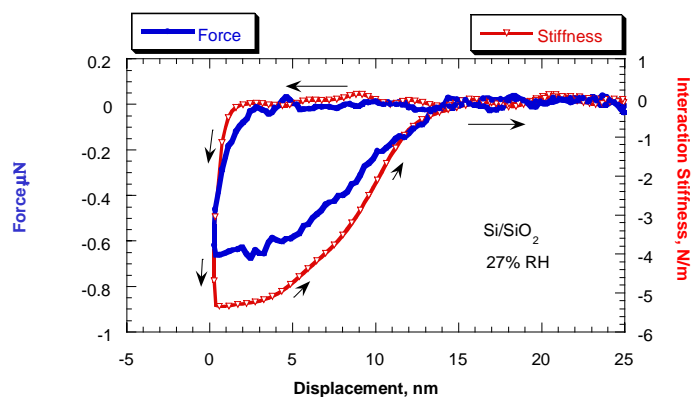


Figure 13. Force-displacement and stiffness-displacement curves showing only attractive interaction.

interaction to be probed while avoiding the problem called "jump-to-contact" experienced in AFM when cantilevers with low stiffness are used. Fig. 13 shows force and stiffness vs. displacement curves for a Si surface with native oxide in 27% RH environment. Both force and stiffness data are consistent with a purely attractive interaction.

Hydrophobic/Hydrophilic Si Surfaces and Humidity

The above spectroscopic techniques were used to examine tip-surface interactions between the diamond indenter and hydrophobic and hydrophilic Si surfaces (38). Surfaces were prepared as hydrophobic using a HF etch and hydrophilic by pirhana etch; oxide film thickness of the treatments were measured by ellipsometry to be 1 nm and 5 nm, respectively. Numerous stiffness-displacement curves were obtained for the as prepared surfaces in dry (<2% RH) conditions, and as the humidity was increased, then decreased. Adhesion interaction lengths (pull-off lengths) were determined from the stiffness-displacement curves by evaluating the distance between the point of contact (0 nm displacement in Fig. 11) and the distance where the interaction stiffness returned to 0 N/m during retraction of the tip from the surface (50 nm in Fig. 11). The top two plots shown in Fig. 14 show the measured pull-off lengths for both surface treatments at various humidities. The pull-off lengths varied considerably depending on surface treatment and humidity, and can be attributed to meniscus formation. The effects of humidity were much greater for the hydrophilic surface, where pull-off lengths were an order of magnitude larger above 60% RH. An estimate of changes occurring in the mechanical properties of the surfaces during these experiments was obtained by examining the ratio of the stiffness (K) vs. the penetration depth (h) (obtained from the repulsive regime, to the left of 0 nm as in Fig 11); this ratio, K/h, is proportional to the reduced modulus of the surface/indenter and is plotted in Fig. 14

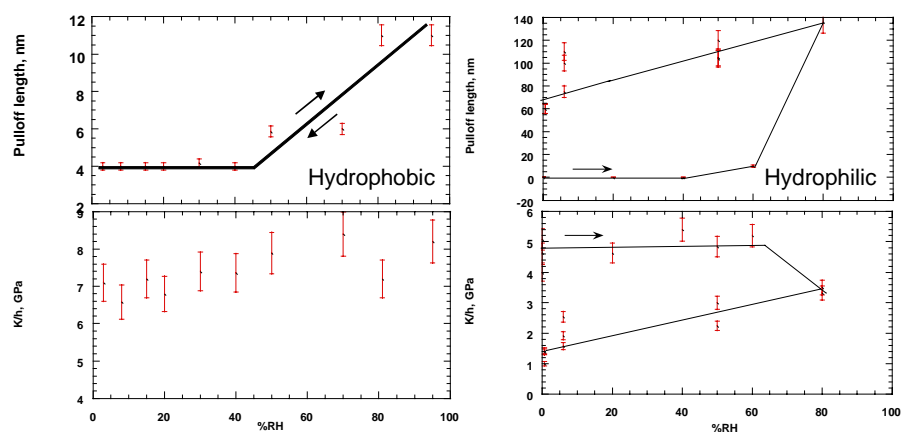


Figure 14. Influence of humidity on pull-off length and ratio of stiffness/penetration depth for hydrophobic (left) and hydrophilic (right) Si/SiO₂ surfaces.

(lower left and right plots) for hydrophobic and hydrophilic surfaces. The stiffness-penetration ratio for the hydrophobic surface did not change appreciably with exposure to humidity, while the hydrophilic surface showed a clear, irreversible reduction in K/h ratio.

For both pull-off length and K/h ratio, the behavior of the hydrophobic surface was fully reversible when humidity was removed. On the other hand, the irreversibility of the hydrophilic surfaces pull-off lengths suggests that water remained on these surfaces. The reduced K/h ratio for the hydrophilic surfaces indicates a lower reduced modulus, suggesting that the surface oxide film has been modified by the exposure to water vapor. Whether the oxide layer became thicker or could be returned to the initial state by heating to drive off adsorbed water was not examined. Low-load indentation experiments demonstrated that these 1-5 nm oxide films altered the indentation behavior of Si surfaces (38).

Mapping the Surface: Stiffness Imaging

The examples presented above are all single point measurements and do not fully take advantage of the scanning capabilities provided by the AFM base. Ideally, one would like to produce an image of sample properties (e.g. map modulus and loss properties) quantitatively and quickly, in an image format. One approach would be to collect multiple force-distance curves over the sample area. This technique of force-curve mapping (41) is very time consuming (a separate force-distance curve is made for each data point in an image) even if the force curves are made rapidly; additionally, materials with time dependent behavior would prove difficult to study.

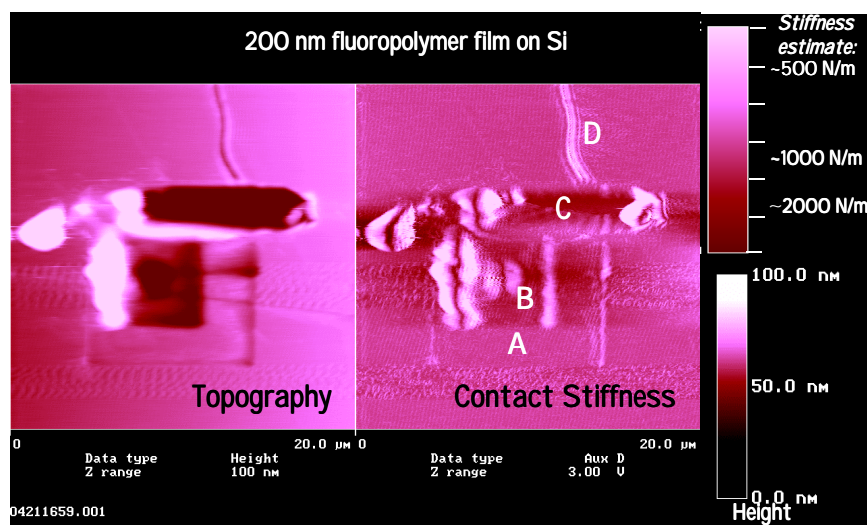


Figure 15. Topography (left) and contact stiffness (right) images obtained of 200 nm thick fluoropolymer film on Si using 300 nN AC force modulation at 200 Hz.

Applying the force modulation technique discussed in this paper with the nanoindenter is possible, but would be particularly inefficient as the force-distance curve acquisition is slow due to the low modulation frequency applied (~ 100 Hz). Instead, we have chosen to apply the modulated force during contact mode imaging (42). Specifically, during contact mode imaging a $\sim 1\mu\text{N}$ force is applied to the sample. On top of that force, we superimpose a small AC modulated force (10-300 nN). By monitoring amplitude response (Δx), the stiffness of the contact ($\Delta F/\Delta x$) can be obtained in an image format, alongside topographic data.

An example is shown in Fig. 15. The image is of a thin (200 nm thick) fluoropolymer film deposited on Si via plasma enhanced chemical vapor deposition (PECVD) (43). On the left side of the image is topography data and on the right, the corresponding displacement response of the contact. Contrast in the stiffness image is due to displacement response to the modulated force and is therefore inverted (dark features are higher stiffness and bright features are lower in stiffness). The features in the image were generated by damaging the film, which was uniform and featureless before scanning. The topography image shows regions of thinned film (A) and heavily damaged film (B,C), and a scratch (D). The contact stiffness image reveals all of these features. For example, topography effects on contact area are seen in the edge effects in the image. The stiffness image contrast in and out of the slightly worn area (A) are similar, indicating similar materials properties. Bright regions in the image reveal debris pile up and delamination of the film, and the dark region in the center of the image is consistent with thinning or removal of the film.

The quantitative stiffness image above provides a first step towards quantitative mapping of modulus and loss properties of surfaces. Difficulties to overcome in converting the stiffness data to elastic modulus arise from the need to know the tip-sample penetration at each point in the image, and to mask the low frequency AC modulation from the scanning feedback electronics. Despite these difficulties, such scanning techniques provide great promise towards the goal of quantitative mechanical properties measurements of surfaces.

Summary

This paper summarizes work in nanomechanics using AC force modulation conducted at NRL. It represents recent progress on the way to a goal of *quantitative, dynamic* measurements of surface mechanical properties and nanoscale sliding contacts. Through the examples given, we have demonstrated quantitative, surface sensitive nanomechanics of thin films and compliant polymers, and the ability to examine damping losses and the effects of water vapor. Finally, new, more powerful techniques such as stiffness imaging hold the promise of quantitative mechanical properties mapping at the nanoscale.

Acknowledgements

The authors are grateful for the contributions of Dr. Odin Warren and Hysitron, Inc., Ken Lee (Geo Centers) and the gift of samples from Dr. Edmund Winder and Prof. Karen Gleason (MIT). We acknowledge the support of the Office of Naval Research (ONR) and Air Force Office of Scientific Research (AFOSR).

References

1. Pethica, J. B.; Hutchings, R.; Oliver, W. C. *Philos. Mag. A* **1983**, 48, 593.
2. Binnig, G.; Quate, C. F.; Gerber, Ch. H. *Phys. Rev. Lett.* **1986**, 56, 930.
3. Pethica, J. B.; Oliver, W. B. *Phys. Scr.* **1987**, T19, 61.
4. Tonck, A.; George, J. M.; Loubet, J.-L. *J. Coll. Int. Sci.* **1988**, 126, 150.
5. Carpick, R. W.; Ogletree, D. F.; Salmeron, M. *Appl. Phys. Lett.* **1997**, 70, 1548.
6. Lantz, M. A.; O'Shea, S. J.; Hoole, A. C. F.; Welland, M. E.; Johnson, K. L. *Phys. Rev. B* **1997**, 55, 10776.
7. Zhong, Q.; Innis, D.; Kjoller, K.; Elings, V.B. *Surf. Sci. Lett.* **1993**, 290, L688.
8. Asif, S. A. S., Thesis, 1997 (Oxford, UK).
9. Wahl, K. J.; Stepnowski, S. V.; Unertl, W.N. *Tribol. Lett.* **1998**, 5, 103.
10. Bhushan, B.; Kulkarni, A. V.; Bonin, W.; Wyrobek, J. T. *Philos. Mag. A* **1996**, 74, 1117.
11. Stephen, A. J.; Houston, J. E. *Rev. Sci. Instrum.* **1990**, 62, 710.
12. Asif, S. A. S.; Wahl, K. J.; Colton, R. J. *Rev. Sci. Instrum.* **1999**, 70, 2408.
13. Tabor, D. *The Hardness of Metals*, Oxford: London, 1951.
14. Oliver, W. C.; Pharr, G. M. *J. Mater. Res.* **1992**, 7, 1564.
15. Asif, S. A. S.; Pethica, J. B. *Phil. Mag. A* **1997**, 76, 1105.
16. Asif, S. A. S.; Pethica, J. B. *J. Adhesion* **1998**, 67, 153.
17. Doerner, M. F.; Nix, W. D. *J. Mater. Res.* **1986**, 1, 601.
18. Burnham, N. A.; Colton, R.J. *Scanning Tunneling Microscopy and Spectroscopy: Theory, Techniques and Applications*; Ed. D. A. Bonnell; VCH Publishers, Inc., New York, NY, 1993, Chapter 7, p.232.
19. Burnham, N. A.; Colton, R.J. *J. Vac. Sci. Technol. A* **1989**, 7, 2906.
20. VanLandingham, M. R.; McKnight, S. H.; Palmese, G. R.; Eduljee, R. F.; Gillespie, J. W., Jr.; McCulough, R. L. *J. Mater. Sci. Lett.* **1997**, 16, 117.
21. VanLandingham, M. *Microscopy Today* **1997**, 97, 12.
22. VanLandingham, M. R.; McKnight, S.H.; Palmese, G.R.; Elings, J. R.; Huang, X.; Bogetti, T. A.; Eduljee, R. F.; Gillespie, J. W., Jr. *J. Adhesion* **1997**, 64, 31.
23. Hues, S. M.; Draper, C. F.; Lee, K. P.; Colton, R. J. *Rev. Sci. Instrum.* **1994**, 65, 1561.
24. Burnham, N. A.; Colton, R. J.; Pollock, H. M. *Nanotechnology* **1993**, 4, 64.
25. Briscoe, B. J.; Fiori, L.; Pelillo, E. *J. Phys. D: Appl. Phys.* **1998**, 31, 2395.
26. Kolosov, O.; Yamanaka, K. *Jpn. J. Appl. Phys.* **1993**, 32, L1095.

27. Kajiyama, T.; Tanaka, K.; Ohki, I.; Ge, S.-R.; Yoon, J.-S.; Takahara, A. *Macromolecules* **1994**, 27, 7932.
28. Overney, R. M.; Meyer, E.; Frommer, J.; Güntherodt, H.-J.; Fujihira, M.; Takano, H.; Gotoh, Y. *Langmuir* **1994**, 10, 1281.
29. Burnham, N. A.; Kulik, A. J.; Gremaud, G.; Gallo, P.-J.; Oulevey, F. *J. Vac. Sci. Technol. B* **1996**, 14, 794.
30. Maivald, P.; Butt, H. J.; Gould, S. A. C.; Prater, C. B.; Drake, B.; Gurley, J. A.; Elings, V. B.; Hansma, P. K. *Nanotechnol.* **1991**, 2, 103.
31. Burnham, N. A.; Gremaud, G.; Kulik, A. J.; Gallo, P.-J.; Oulevey, F. *J. Vac. Sci. Technol. B* **1996**, 14, 1308.
32. Tanaka, K.; Taura, A.; Ge, S.-R.; Takahara, A.; Kajiyama, T. *Macromolecules* **1996**, 29, 3040.
33. Overney, R.M.; Leta, D.P.; Pictroski, C.F.; Rafailovich, M.H.; Liu, Y.; Quinn, J.; Sokolov, J.; Eisenberg, A.; and Overney, G. *Phys. Rev. Lett.* **1996**, 76, 1272.
34. Jarvis, S.P.; Weihs, T.P.; Oral, A.; Pethica, J. B. *Thin Films: Stresses and Mechanical Properties IV*, MRS Symposium Proceedings; MRS: Pittsburgh, PA, 1993, Vol. 308; pp127-132.
35. Jarvis, S.P.; Weihs, T.P.; Oral, A.; Pethica, J. B. *Rev. Sci. Instrum.* **1993**, 64, 3155.
36. Pyne, A. R.; *Rheology of Elastomers*; Pergamon Press: London, 1958.
37. Loubet, J. L.; Lucas, B. N.; Oliver, W. C. *NIST Special Publication No. 896*; National Institute of Standards and Technology, Gaithersburg, MD, 1996.
38. Asif, S. A. S.; Wahl, K. J.; Colton, R. J. *J. Mater. Res.* **2000**, 15, 546.
39. Israelachvili, J.N.; Tabor, D. *Proc. R. Soc. London Ser. A* **1972**, 331, 19.
40. Israelachvili, J.N. *Intermolecular and Surface Forces*; Academic Press: New York, NY, 1991; p.164.
41. Koleske, D.D.; Lee, G. U; Gans, B. I.; Lee, K. P.; DiLella, D. P.; Wahl, K. J.; Barger, W. R.; Whitman, L. J.; Colton, R. J. *Rev. Sci. Instrum.* **1995**, 66, 4566.
42. Asif, S. A. S.; Wahl, K. J.; Colton, R. J., *Thin Films: Stresses and Mechanical Properties VIII*, MRS Symposium Proceedings; MRS: Pittsburgh, PA, 2000, Vol. 594, in press.
43. Labelle, C. B.; Gleason, K. K. *J. Vac. Sci. Technol. A* **1999**, 17, 445.